2023 IEEE International Conference on Robotics and Automation (ICRA 2023)
May 29 - June 2, 2023. London, UK

# Evaluating the Feasibility of Magnetic Tools for the Minimum Dynamic Requirements of Microneurosurgery

Cameron Forbrigger, Erik Fredin, and Eric Diller

***Abstract*— Neurosurgery could benefit from robot-assisted minimally invasive approaches, but existing robot tools are insufficiently small and compact. Magnetic actuation is an attractive approach to medical robotics because it allows small, modular serial mechanisms to be remotely actuated. Despite these advantages, magnetic actuation is relatively weak compared to alternative actuation methods. In this paper, we introduce a novel analytical model for magnetic serial robots, use this model to design two prototypes, and then demonstrate that a 4-mm-diameter prototype without any internal mechanical transmission can produce forces up to 0.181 N: high enough to perform delicate microsurgical tasks. We also demonstrate that the robot can achieve a closed-loop step response rise time of 0.71 seconds with an overshoot of 7.8%: sufficiently fast for surgical motions while maintaining a tip precision of less than 2 mm during a worst-case dynamic motion. These experiments provide strong evidence for the feasibility of directly-driven magnetic tools for neurosurgical applications, and they motivate future investigations in this area.**

## I. INTRODUCTION

Interest in robotic approaches to minimally-invasive (endoscopic) neurosurgery is high, with hopes that it will yield greater tool stability, provide haptic feedback and neuronavigation, and improve the physical comfort of the surgeon operator during long and arduous procedures [1], [2]. While robot-assisted endoscopes and catheters have been developed for neurosurgical tasks, wristed robotic tools that are sufficiently small and compact for this highly constrained environment are yet to be developed.

Magnetically-actuated devices present an attractive approach to minimally-invasive medical tasks due to their wireless power delivery [3]. Interest in magnetic devices for medicine centers around steering catheters [4], laser tools [5], and endoscopes [6] and navigating magnetic micro/nanoagents [7] or capsule robots [8], but little investigation has been performed into devices for performing neurosurgical tasks [9]–[11]. There is a perception that magnetic devices have insufficient force capabilities for most surgical tasks [12]. Efforts to increase the output strength of magnetically-actuated devices show some recent progress with mm-scale mechanical transmissions [13], [14]. However, transmissions increase the complexity of tool designs, invariably leading to more potential points of failure. A magnetic device design without a mechanical transmission would therefore be advantageous, but only if it can meet the dynamic requirements of the target procedure.

This work was supported in part by the Natural Sciences and Engineering Research Council of Canada through the Discovery Grant Program 2014-04703 and in part by the Canadian Institutes for Health Research under Grant CPG-158271. (*Corresponding author: Eric Diller.*)

Department of Mechanical and Industrial Engineering, University of Toronto, 5 King's College Rd, Toronto, ON M5S 3G8 ediller@mie.utoronto.ca

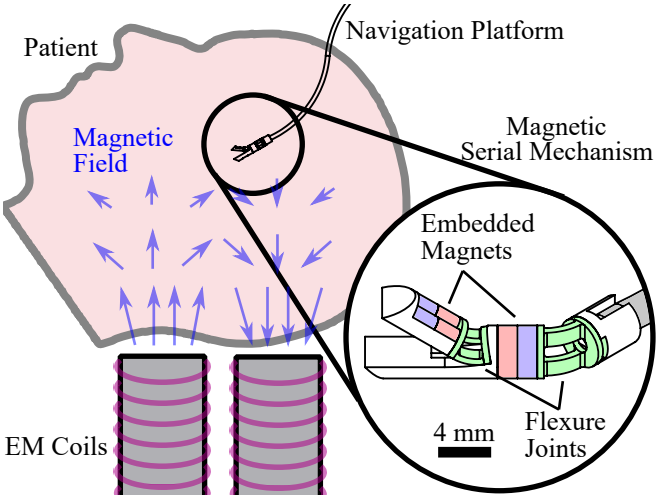


Fig. 1. Concept of the magnetic serial robot, composed of a coil system and a magnetic serial mechanism mounted on a flexible navigation platform.

A magnetic serial robot (MSR) that is directly driven by magnetic fields (i.e. no mechanical transmission, is illustrated in Fig. 1. The MSR consists of a serial mechanism with embedded magnetic material in the mechanism links and a system for modulating the magnetic field in the workspace of the serial mechanism (e.g. electromagnetic coils). By modulating the direction, magnitude, and spatial gradient of the magnetic field in the workspace, we can control the force and torque on the magnetic material in the mechanism links. In Fig. 1 the magnetic serial mechanism is shown being navigated to the target location by a continuum robot, but the wireless nature of magnetic actuation makes the MSR completely modular: the navigation plaform could be as simple as a plastic rod, or as complex as a flexible endoscope.

The objective of this study is to demonstrate that magnetic, millimeter-scale devices can meet the minimum dynamic requirements needed to be feasible for microneurosurgical tasks. Microneurosurgery involves delicate manipulation compared to other surgical domains [15], so it is well-suited to low-force devices. First we define minimum force and speed requirements for neurosurgical tools by referencing existing literature. Then we develop a novel general analytical model for magnetic serial mechanisms that is used to design a rigid link and flexible link 4-mm-diameter magnetic prototype. We have formulated a simple closed loop con-

troller that accounts for the control-affine nonlinear dynamics of the magnetic serial robot prototypes. These prototypes are then evaluated against the force and speed requirements while being actuated with a clinical-scale electromagnetic coil system. The mechanism designs presented here are extensions of our previous work in [11], [16].

### A. Minimum Dynamic Requirements for Microneurosurgery

There is a lack of quantitative biomedical/biomechanical literature on the forces, velocities, and accelerations of tools during neurosurgery, which makes it very challenging to produce specific and measurable design requirements for surgical robots. In this section we cite the few existing studies on the topic of neurosurgical dynamics and develop minimum requirements that can be used as a feasibility measure for new robot tools.

Marcus *et al.* [15] measured forces exerted during a sequence of three microneurosurgical procedures in ten different regions of a cadaver brain: starting an incision with a scalpel, carrying (continuing) the incision for 30 mm, and retracting (pulling apart) the completed incision to a distance of 5 mm. The median forces for 25 out of the 26 procedures were $\leq 0.18$ N, with the one exception being carrying an incision in the corpus callosum (0.23 N). If we assume the median forces from [15] to be representative of reasonable force requirements, then tools for microsurgery need to be able to exert forces in the range of 0.1 to 0.2 N. These numbers are a reasonable target, given that the same study also found iatrogenic (unintended) injury was more likely to occur when forces exceeded 0.22 N [15].

Maddahi *et al.* [17] measured the position, orientation, and forces applied by a bipolar forceps tool operated by a trained neurosurgeon during open surgery on cadaver brains during the dissection and coagulation of different regions. The frequency range of the tool movements and applied forces were 3 Hz and 5 Hz, respectively. These frequency ranges indicate that the feedback method for a surgical robot should acquire at a minimum rate of 10 Hz to satisfy the Nyquist criterion, with an ideal feedback method providing at least 25 Hz. These frequency ranges also suggest that the dynamic response of the tool should be on the order of tenths of a second. This conclusion corresponds well with feedback from our own discussions with neurosurgeons, who commented that robot designs with rise times of greater than 1 s felt "sluggish." As a result, we have chosen a closed loop step response rise time target of $t_r < 1.0$ s with a maximum allowable overshoot of $M_p < 10\%$. A faster response is preferred, but overshoot should be low for safety reasons. A step change in the desired robot pose is unlikely to ever be intentionally requested by a surgeon; therefore, the step response represents the worst-case dynamic motion.

## II. Dynamic Model of a Magnetic Serial Robot

The relationship between the field and the equivalent torque about each joint in the mechanism is not always obvious, especially when magnetic gradients are non-zero. A model is needed to determine what fields are necessary to produce the desired torques to accurately control the MSR. Our main theoretical contribution lies in deriving a general dynamic model for the control of magnetic serial robots.

### A. Equation of Motion for Serial Robots

The equation of motion of an $n$-link serial robot in joint-space formulation [18] is

$$H\ddot{\boldsymbol{q}} = \boldsymbol{\tau}_C(\dot{\boldsymbol{q}}, \boldsymbol{q}) + \boldsymbol{\tau}_K(\boldsymbol{q}) + \boldsymbol{\tau}_U(\boldsymbol{u}), \tag{1}$$

where $\boldsymbol{q}$ is an $n \times 1$ vector of the generalized coordinates of the robot (m and rad), $\dot{\boldsymbol{q}}$, and $\ddot{\boldsymbol{q}}$ are the first and second partial derivatives of $\boldsymbol{q}$ with respect to time; $H$ is the $n \times n$ generalized (joint space) inertia matrix (kg and kg·m$^2$); $\boldsymbol{\tau}_C$ is a vector of velocity-dependent generalized forces (N and N·m), including the fictitious forces introduced by the non-inertial reference frames of the joint space formulation (centrifugal and coriolis); $\boldsymbol{\tau}_K$ is a vector of position-dependent generalized forces, such as those due to gravity or joint stiffness; and $\boldsymbol{\tau}_U$ is the generalized forces due to the actuators of the robot, which is a function of the $p$ control inputs contained as elements of the vector $\boldsymbol{u}$.

### B. Magnetic Field in the Robot Workspace

Unlike conventional serial robots, magnetic serial robots do not have individual actuators dedicated to each joint. Instead, embedded magnets experience forces and torques (combined into a single $6 \times 1$ column vector called a wrench $\mathfrak{w}$) due to the magnetic field $\boldsymbol{b} = (b_x, b_y, b_z)$ present in the robot workspace. In robotics applications, it is convenient to represent the magnetic field using the $8 \times 1$ augmented field vector that includes five independent field gradients [19]:

$$\boldsymbol{\beta} = \begin{bmatrix} b_x & b_y & b_z & \frac{\partial b_x}{\partial x} & \frac{\partial b_x}{\partial y} & \frac{\partial b_x}{\partial z} & \frac{\partial b_y}{\partial y} & \frac{\partial b_y}{\partial z} \end{bmatrix}^{\mathsf{T}}. \tag{2}$$

In an MSR, there are two sources of magnetic field that need to be accounted for: 1) the magnetic field due to the actuation system $\boldsymbol{\beta}_U(\boldsymbol{u})$, and 2) the magnetic field from the magnetic volumes in each of the links $\sum_{k=0}^{n} \boldsymbol{\beta}_k$. Fortunately, magnetic fields superimpose linearly in air, which allows the magnetic field at any position vector $\boldsymbol{r}$ to be determined:

$$\boldsymbol{\beta}(\boldsymbol{r}) = \boldsymbol{\beta}_U(\boldsymbol{u}, \boldsymbol{r}) + \sum_{k=0}^{n} \boldsymbol{\beta}_k(\boldsymbol{m}_k, \boldsymbol{r} - \boldsymbol{r}_k). \tag{3}$$

In (3) we have made our first simplifying assumption: the point dipole assumption allows us to model the magnetic material in each link as a single $3 \times 1$ vector quantity $\boldsymbol{m}_k$ located at the centroid $\boldsymbol{r}_k$ of the magnetic volume.

### C. Magnetic Wrench on Each Embedded Magnet

The $6 \times 1$ magnetic wrench $\mathfrak{w}_j = \left[\boldsymbol{f}_j; \boldsymbol{t}_{O,j}\right]$ on the point dipole in the $j^{\text{th}}$ link can be determined using

$$\begin{aligned} \mathfrak{w}_j &= \begin{bmatrix} 0_{3\times3} & M_f(\boldsymbol{m}_j) \\ S\{\boldsymbol{m}_j\} & S\{\boldsymbol{r}_j\} M_f(\boldsymbol{m}_j) \end{bmatrix} \boldsymbol{\beta}(\boldsymbol{r}_j), \\ \mathfrak{w}_j &= M_w(\boldsymbol{m}_j, \boldsymbol{r}_j) \boldsymbol{\beta}(\boldsymbol{r}_j), \end{aligned} \tag{4}$$

where $\boldsymbol{f}_j$ is the magnetic force on the magnetic dipole; $\boldsymbol{t}_{O,j}$ is the magnetic torque on the magnetic dipole about the origin of the reference frame;

$$M_f(\boldsymbol{m}) = \begin{bmatrix} m_x & m_y & m_z & 0 & 0 \\ 0 & m_x & 0 & m_y & m_z \\ -m_z & 0 & m_x & -m_z & m_y \end{bmatrix}, \tag{5}$$

is the magnetic force matrix [19]; and

$$S\{\boldsymbol{a}\}\boldsymbol{b} = \begin{bmatrix} 0 & -a_z & a_y \\ a_z & 0 & -a_x \\ -a_y & a_x & 0 \end{bmatrix} \boldsymbol{b} = \boldsymbol{a} \times \boldsymbol{b}, \tag{6}$$

is the skew-symmetric matrix form of the vector cross-product.

The magnitude of each magnetic dipole $\boldsymbol{m}_j$ is constant, and its orientation $\hat{\boldsymbol{m}}_j$ and position $\boldsymbol{r}_j$ are solely functions of the present robot configuration. As a result, by combining equations (3) and (4) we can write

$$\mathfrak{w}_j = M_w(\boldsymbol{q})\boldsymbol{\beta}_U(\boldsymbol{u}) + M_w(\boldsymbol{q}) \sum_{k=0}^{n} \boldsymbol{\beta}_k(\boldsymbol{q}). \tag{7}$$

In (7) we have made our second simplifying assumption: we assume that the augmented field vector $\boldsymbol{\beta}_U$ produced by the field actuation system is constant throughout the serial mechanism workspace ("homogeneous field assumption" [19]). As a result, we can see that the magnetic wrench on each dipole in the serial mechanism can be divided into a wrench that is a function of the control inputs $\mathfrak{w}_{U,j}$ and an internal wrench between embedded dipoles $\mathfrak{w}_{int,j}$ that is solely a function of the robot configuration $\boldsymbol{q}$.

$$\mathfrak{w}_j = \mathfrak{w}_{U,j}(\boldsymbol{q},\boldsymbol{u}) + \mathfrak{w}_{int,j}(\boldsymbol{q}) \tag{8}$$

The internal wrench can be thought of as a magnetic spring, so it can be encapsulated in the $\boldsymbol{\tau}_K(\boldsymbol{q})$ term in (1). Designing these magnetic springs to produce useful behaviours is discussed in [16], [20], [21].

### D. Generalized Forces Acting About the Joints

The scalar actuating generalized force about the $i^{\text{th}}$ joint $\tau_{U,i}$ can be determined from the sum of actuating wrenches $\mathfrak{w}_{U,j}$ acting on all links distal to the $i^{\text{th}}$ joint [18]:

$$\tau_{U,i} = \mathfrak{t}_i^{\mathsf{T}} [\Delta] \sum_{j=i}^{n} \mathfrak{w}_{U,j}, \tag{9}$$

where

$$[\Delta] = \begin{bmatrix} 0_{3\times3} & I_{3\times3} \\ I_{3\times3} & 0_{3\times3} \end{bmatrix},$$

and $\mathfrak{t}_{t,i} = [\boldsymbol{\omega}_i; \boldsymbol{v}_{O,i}]$ is the twist of unit amplitude corresponding to the $i^{\text{th}}$ joint. If the local reference frames of each link are defined according to the Denavit-Hartenberg convention, then the twist can be determined using

$$\mathfrak{t}_i = \begin{bmatrix} \hat{\boldsymbol{z}}_{i-1} \\ \boldsymbol{o}_{i-1} \times \hat{\boldsymbol{z}}_{i-1} \end{bmatrix} \tag{10}$$

for a revolute joint or

$$\mathfrak{t}_i = \begin{bmatrix} 0_{3\times1} \\ \hat{\boldsymbol{z}}_{i-1} \end{bmatrix} \tag{11}$$

for a prismatic joint, where $\hat{\boldsymbol{z}}_{i-1}$ is the $z$-axis unit vector and $\boldsymbol{o}_{i-1}$ is the origin of the $(i-1)^{\text{th}}$ link's reference frame.

By inserting the expression for $\mathfrak{w}_{U,j}$ from (7) into (9), the individual scalar generalized forces can be combined into a single vector expression:

$$\boldsymbol{\tau}_U(\boldsymbol{q},\boldsymbol{u}) = M_\beta(\boldsymbol{q})\boldsymbol{\beta}_U(\boldsymbol{u}), \tag{12}$$

where $M_\beta$ is the $n \times 8$ magnetic actuation matrix.

### E. Field Modulation System Model

In the case of a system of $p$ stationary electromagnets, given the homogeneous field assumption made previously in Section II-C, the augmented field vector can be modeled as a linear function of the coil currents:

$$\boldsymbol{\beta}_U = M_{coil}\boldsymbol{u}, \tag{13}$$

where $M_{coil}$ is the constant $8 \times p$ coil calibration matrix [19]. This model becomes less accurate for electromagnets with soft magnetic cores as the cores reach magnetic saturation.

By inserting (13) into (12) we arrive at the final expression for the actuation dynamics of the magnetic serial robot:

$$\boldsymbol{\tau}_U(\boldsymbol{q},\boldsymbol{u}) = B(\boldsymbol{q})\boldsymbol{u}, \tag{14}$$

where $B(\boldsymbol{q}) = M_\beta M_{coil}$ is the $n \times p$ current actuation matrix.

### F. Discussion of the Analytical Model

From (14) we can see that the MSR dynamics are affine with respect to $\boldsymbol{u}$ despite being nonlinear with respect to $\boldsymbol{q}$. We can also see that $\text{rank}(B) \leq 8$ because $\text{rank}(M_{coil}) \leq 8$; this conclusion is consistent with other works on the magnetic actuation of parallel mechanisms [22]. If $\text{rank}(B) < n$ (i.e. lacks full row rank), then the MSR is underactuated. Underactuation is not a problem in some robotics applications, but would be considered undesirable in surgical applications: an underactuated system cannot undergo arbitrary state transitions, so the surgeon operator would have a limited choice of non-obvious trajectories to move to a new state. Therefore, a good MSR design ensures that $B$ has full row rank for all $\boldsymbol{q}$ in the robot jointspace.

A design methodology for MSR that maximizes their independence between their DOF, similar to what has been previously done for parallel magnetic mechanisms [22], is beyond the scope of this study, but the mechanisms shown in Section IV-A were designed to have full row rank in all configurations. This design problem becomes increasingly challenging with increasing numbers of links and is the subject of future work.

## III. Closed Loop Control Strategy

The model derived in Section II could enable a variety of nonlinear control schemes, such as the computed torque method [23]. However, for this study we used a relatively simple joint-space PID controller to achieve the desired joint-space dynamics because it is less sensitive to modeling errors compared to more complex nonlinear controllers. Investigating control performance improvements with more complex control schemes is an area of future work.

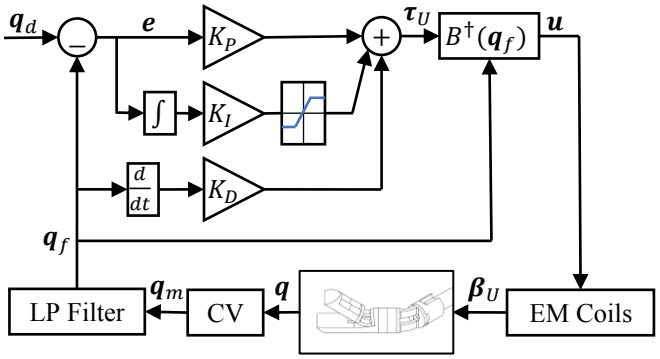


Fig. 2. Control algorithm schematic

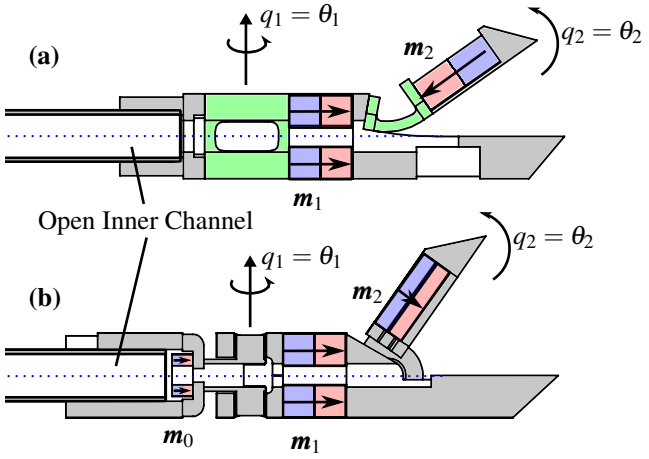


Fig. 3. A schematic showing a section view of a) Design S with flexure joints (green highlighted components) and b) Design U with rigid joints, with the magnetization directions and joint values of both designs indicated.

The control schematic is shown in Fig. 2. A computer vision system produces a measurement $\boldsymbol{q}_m$ of the robot configuration, which is passed through a low-pass filter to yield $\boldsymbol{q}_f$. The configuration error $\boldsymbol{e}$ is then determined. A PID controller is used to calculate a desired value for $\boldsymbol{\tau}_U$ based on $\boldsymbol{e}$. The filtered value of the configuration $\boldsymbol{q}_f$ is calculated using a moving average width of 15 time steps ($\Delta t \approx 2$ ms). Saturation is applied to prevent integral wind-up.

The electromagnet currents $\boldsymbol{u}$ required to apply the desired torques $\boldsymbol{\tau}_U$ are determined from a linear least-squares (LLS) solution to the linear system described by (14) using the complete orthogonal decomposition algorithm from the open-source C++ library Eigen v3.4.0 [24]. The desired currents commands $\boldsymbol{u}$ are then sent to the amplifiers that drive the stationary electromagnetic coil system. The eight coils in the electromagnet system we used were designed to have identical impedance, so the linear least-squares solution for the coil currents corresponds to the most power-efficient solution [19] to achieve the desired generalized forces.

## IV. Magnetic Serial Robot Prototype

### A. Magnetic Serial Mechanisms

Two different magnetic serial mechanism designs, illustrated in Fig. 3, were investigated to produce a gripper with one rotary wrist joint and one rotary finger joint. The first gripper design (Design S) uses flexure joints, and the second gripper design (Design U) uses rigid pin joints. We modeled the flexure joints as short length flexural pivots [25]. The two designs were chosen to demonstrate the significant effect that the magnetization orientation has on the force output of the tools (see Section V).

A FormLabs Form3 printer with ClearV4 resin was used to form the rigid sections of both designs, and Flexible80A resin was used to form the flexure joints. The embedded magnetic volumes used in both designs were neodymium magnets from SM magnetics: a Tube0077 N40 NdFeB magnet ($\|\boldsymbol{m}\| \approx 35.9$ mA·m$^2$) for $\boldsymbol{m}_1$ for both designs, an M0404 N50 arc magnet ($\|\boldsymbol{m}\| \approx 26.8$ mA·m$^2$) for $\boldsymbol{m}_2$ for Design U, and four D1001B N50 NdFeB magnets ($\|\boldsymbol{m}\| \approx 16.1$ mA·m$^2$) for $\boldsymbol{m}_2$ for Design S. Design U also has a base link magnet $\boldsymbol{m}_0$ that provides a restoring torque on the wrist joint (SM Magnetics R0100) [16], which is unnecessary for Design S because the flexure joint provides a restoring torque.

Both designs have a 1.0 mm diameter inner channel which, while sacrificing some magnetic volume, can allow components such as sensor wires, irrigation tubes, or fiber optic lighting to pass through the center of the robot (see the Supplementary Video). This central channel is a feature unique to magnetic actuation: wireless power delivery means that there are no cables or wires running through the robot, so the extra space is left for other functionality.

Design S has a finger magnet $\boldsymbol{m}_2$ that is magnetized along the length of the finger. The inter-magnetic wrench between the wrist and finger magnets provides a spring-like effect [16] that results in a normally-closed finger configuration. In contrast, Design U has a finger magnet $\boldsymbol{m}_2$ that is magnetized along the thickness of the finger that results in a normally-open finger configuration. The analytical model predicts that Design U should be capable of higher wrist torques, and therefore higher output forces, compared to Design S.

### B. Magnetic Field Modulation System

The experimental apparatus is shown in Fig. 4. A clinical-scale electromagnetic coil system with $p = 8$ electromagnet coils and a large open workspace was used to generate the applied fields (Fig. 4(a)). This system is capable of field strengths up to approximately 0.050 T and field gradients up to approximately 0.5 T/m ($u_{max} = 24$ A) [26]. The serial mechanism was held at the center of the coil workspace on the end of a titanium tube (Fig. 4(b)).

### C. Computer Vision Feedback

Feedback is implemented using two cameras (Fig. 4(a)) and filtering methods using the OpenCV library for C++. Each camera is placed perpendicular to the joint angle that it measures. A binary threshold is applied to each set of frames coming from the cameras, such that a contour and a

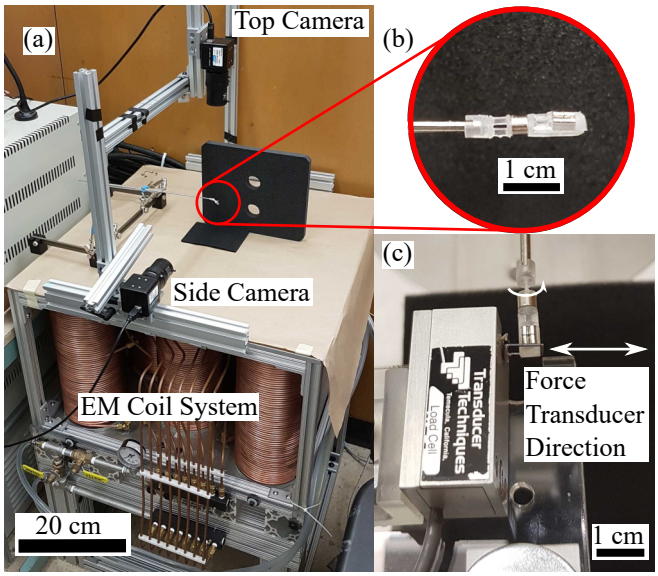


Fig. 4. Overview of the magnetic serial robot design. (a) The electromagnetic coil system with top and side view cameras. A magnetic serial mechanism (b) is held at the tip of a hollow titanium tube. (c) Force testing setup for the wrist force experiments.

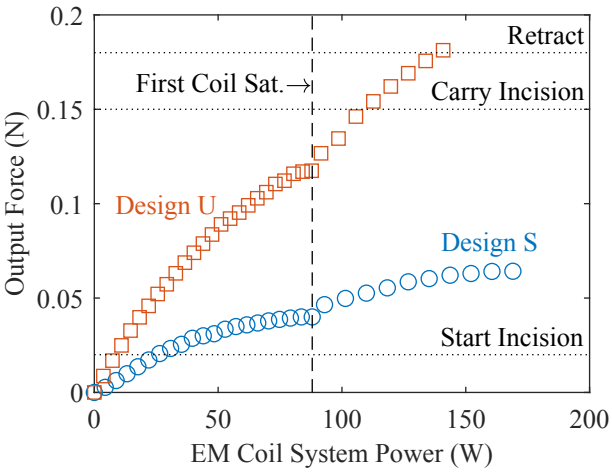


Fig. 5. Gripper wrist blocking force for Design S (closed, weakest config.) and Design U (open, strongest config.) vs. the coil system power.

bounding box of the surgical tool can be deduced. The contour and bounding box are then used together with principal component analysis (PCA) in order to find the orientation of the major axis of each respective link. Estimation errors for the wrist angle range from 1-3°, which can be due to varying lighting conditions and poses of the surgical tool. Camera frames were processed on parallel threads, achieving a measurement rate of 60 Hz, which greatly exceeds the minimum 25 Hz target set in Section I-A. The controller was run in a separate thread from the computer vision and had an update rate of 500 Hz.

## V. Wrist Force Testing

As shown in Fig. 4(c), the base link (link 0) of each gripper design was fixed to a rigid testing jig, with the tip of the gripper placed against the loading point of a GSO-100 series load cell from Transducer Techniques (range of ±981 mN, rated accuracy of ±0.5 mN). Design S was left in its naturally-closed position ($\boldsymbol{q} = \begin{bmatrix}0 & 0\end{bmatrix}^\mathsf{T}$), which the analytical model predicts is the configuration resulting in the weakest wrist torques. Design U was left in its naturally-open position ($\boldsymbol{q} = \begin{bmatrix}0 & 1.05\end{bmatrix}^\mathsf{T}$), which the analytical model predicts is the configuration resulting in the strongest wrist torques. The results of these experiments should then provide upper and lower bounds for the wrist forces of this class of MSR design.

The linear combination of currents $\boldsymbol{u}'$ needed to achieve maximum actuation torque about the wrist joint while maintaining zero torque about the finger joint $\hat{\boldsymbol{\tau}}_U = \begin{bmatrix}1 & 0\end{bmatrix}^\mathsf{T}$ was calculated using the linear least-squares approach described previously. For each force measurement, the current vector was determined using

$$\boldsymbol{u} = \frac{\boldsymbol{u}'}{\|\boldsymbol{u}'\|_\infty} u_f \,, \tag{15}$$

where $\|\cdot\|_\infty$ denotes the infinity-norm and $u_f$ is a scalar current factor. These currents were applied to the gripper with $u_f$ increasing linearly from $0 \le u_f \le 24$ A. The significance of $u_f = 24$ A is that it represents the point at which at least one of the coils has reached its maximum current; therefore, the force produced by currents determined from (15) with $u_f = 24$ A is the maximum force that can be achieved in the wrist while still maintaining zero finger torque $\tau_{U,2} = 0$.

However, the wrist torque $\tau_{U,1}$ can be increased further if no constraints are maintained on the finger torque. In that case, the current vector was determined using

$$\boldsymbol{u} = \text{sign}\,(\boldsymbol{B}_1)\, u_f \,, \tag{16}$$

where $\text{sign}\,(\boldsymbol{B}_1)$ denotes the signum function and $\boldsymbol{B}_1$ is the transpose of the first row of the $B$ matrix (i.e. the row corresponding to the wrist joint). A second set of force measurements were performed for each gripper using the currents determined from (16) with $u_f$ increasing linearly in steps of 1.2 A from $0 \le u_f \le 24$ A.

Fig. 5 plots the measured wrist blocking force for Design S (circular datapoints) and Design U (square datapoints) against the total steady-state coil system power consumption $\sum_{i=1}^{p} u_i^2 R_i$. The vertical dashed line indicates the power at which the constraint on the finger force can no longer be maintained. To simplify the presentation of the results, only the results achieved using the currents determined from (15) are shown to the left of the vertical dashed line. The datapoints to the right of the dashed line were produced by currents determined using the method from (16). The maximum values of the median forces from [15] (excluding the corpus callosum) are shown as dotted horizontal lines.

The maximum forces achieved by both designs are summarized in Table I. Both designs are easily capable of the forces required to start incisions in brain tissue in all regions of the brain measured by [15]. If the finger torque does not need to be constrained, Design U is capable of all procedures in all regions of the brain except for one: carrying an incision

in the corpus callosum. As predicted by the analytical model, Design S is significantly weaker: even without constraints on the finger torque it is only capable of retracting tissue in one of the regions of the brain measured by [15].

While the analytical model predicts a linear increase in output force with respect to input current magnitude, the force data in Fig. 5 show a concave-down trend. The most likely source of this trend is that the the iron cores within the coils enter a less linear region of their magnetization curve at higher currents. This magnetization behaviour was observed during coil calibration [26]. While more complex models of the coils could be used to yield more accurate knowledge of the field in the workspace, the linear model in (13) was found to be sufficient for this study.

## VI. Wrist Control Testing

Design S was used for the control experiments because its magnetization resulted in a stable open-loop wrist response for any finger configuration. In contrast, Design U would become unstable as the finger was closed, and the PID controller was not able to stabilize its dynamics. The Ziegler-Nichols tuning method [27] was used to determine acceptable gains for the PID controller for the wrist of Design S. The final tuning parameters chosen were $K_p = 0.25$ mN/rad, $K_i = 0.55$ mN/rad and $K_d = 0.013$ mN/rad. These tuning parameters yielded the most satisfactory performance for minimizing both rise-time and overshoot in step-responses.

The results of the normalized closed loop step response results for the wrist of Design S with the tuned PID controller are shown in Fig. 6. A total of 15 step responses were recorded, with the input step change varying between $20^\circ \leq H_{step} \leq 120^\circ$. The average rise-time was 0.71 seconds and the average overshoot was 7.8%, while their maximum values were 1.12 seconds and 13%, respectively.

The average values for rise-time and overshoot meet their targets, while the maximum values for both metrics exceed the targets. The highest overshoot occurred for a step change of $H_{step} = 100^\circ$, with smaller step-changes generally resulting in a lower percent overshoot. Rise-times tended to be faster for larger step-changes and slower for smaller step changes. This results shows the nonlinear nature of the dynamics: linear systems should show the same step response rise time regardless of step height.

The length of the tool from the wrist joint to the finger tip was 15 mm; therefore 7.8% overshoot equates to approximately 2 mm of overshoot in the finger tip position after a step change of 90°. Neurosurgery requires sub-millimeter precision, but considering that a neurosurgical robot should be following smooth trajectories rather than step changes in an actual operating scenario, 2 mm is a reasonable amount of tip error. In the supplementary video the gripper is shown being controlled by a human operator with a gamepad, which represents a more realistic dynamic scenario for a surgical robot with teleoperation.

Real-time feedback for small-scale magnetically actuated serial robots is significantly less accurate than for industrial robots, due to the use of computer vision. Varying lighting conditions lead to changing contours being detected even if the surgical tool is still, leading to noisy data. Feedback for the presented experiment had a precision of 1.5°. To address this the measured state was averaged over the previous 15 time steps for each control iteration. This filtering yielded sufficient noise reduction while maintaining an adequate response time. More robust vision methods would eliminate the need for such aggressive filtering.

In addition, we acknowledge the method used for feedback in this experiment is unfeasible for clinical settings. Accurate external feedback is a known and persistent challenge for robot-assisted surgery in confined environments for all classes of robots, not only MSR [28]. Due to space constraints, it is not possible to place two cameras perpendicular to the surgical tool: vision is instead provided by an endoscopic camera with a poorer field of view. Furthermore, computer vision in a surgical environment faces obstacles such as tool occlusion, blood and smoke [29], making the computer vision techniques used in this experiment unfeasible. In the past 10 years, deep-learning based approaches have revolutionized the field of computer vision in general, and have increasingly been adopted for surgical computer vision [30], [31]. Acquiring sufficient datasets to implement deep-learning based visual feedback from a limited endoscope camera view remains an important area of future work.

TABLE I

A summary of maximum forces for each gripper design and the number of regions of the brain in which each procedure can be performed based on the force requirements from [15].

| Design/Finger Condition | $F_{max}$ (N) | Start Incis. | Carry Incis. | Retract |
|---|---|---|---|---|
| S/Constrained | 0.040 | 10/10 | 3/9 | 1/7 |
| S/Unconstrained | 0.064 | 10/10 | 4/9 | 1/7 |
| U/Constrained | 0.117 | 10/10 | 6/9 | 5/7 |
| U/Unconstrained | 0.181 | 10/10 | 8/9 | 7/7 |

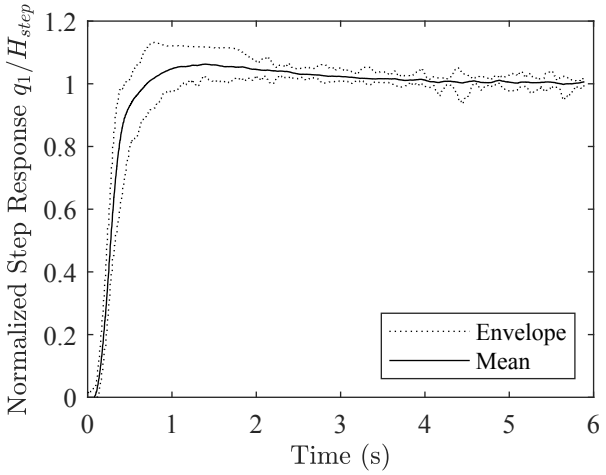


Fig. 6. Normalized step response envelope and mean for N = 15 trials with the Design S prototype.

## REFERENCES


[1] T. Ball, J. González-Martínez, A. Zemmar, A. Sweid, S. Chandra, D. Vansickle, J. S. Neimat, P. Jabbour, and C. Wu, "Robotic applications in cranial neurosurgery: Current and future," *Operative Neurosurgery*, vol. 21, pp. 371–379, Dec. 2021.

[2] A. Attanasio, B. Scaglioni, E. D. Momi, P. Fiorini, and P. Valdastri, "Autonomy in surgical robotics," *Annual Review of Control, Robotics, and Autonomous Systems*, vol. 4, pp. 651–679, 2021.

[3] L. Sliker, G. Ciuti, M. Rentschler, and A. Menciassi, "Magnetically driven medical devices: A review," *Expert Review of Medical Devices*, vol. 12, no. 6, pp. 737–752, 2015.

[4] J. Hwang, J. young Kim, and H. Choi, "A review of magnetic actuation systems and magnetically actuated guidewire- and catheter-based microrobots for vascular interventions," *Intelligent Service Robotics*, vol. 13, pp. 1–14, 2020. [Online]. Available: https://doi.org/10.1007/s11370-020-00311-0

[5] S. Gervasoni, J. Lussi, S. Viviani, Q. Boehler, N. Ochsenbein, U. Moehrlen, and B. J. Nelson, "Magnetically assisted robotic fetal surgery for the treatment of spina bifida," *IEEE Transactions on Medical Robotics and Bionics*, vol. 4, pp. 85–93, 2022.

[6] G. Pittiglio, P. Lloyd, T. da Veiga, O. Onaizah, C. Pompili, J. H. Chandler, and P. Valdastri, "Patient-specific magnetic catheters for atraumatic autonomous endoscopy," *Soft robotics*, vol. 9, pp. 1120–1133, 12 2022.

[7] T. Gwisai, N. Mirkhani, M. G. Christiansen, T. T. Nguyen, V. Ling, and S. Schuerle, "Magnetic torque-driven living microrobots for increased tumor infiltration," *Science Robotics*, vol. 7, pp. eabo0665(1–15), 2022.

[8] J. Nam, Y. P. Lai, L. Gauthier, G. Jang, and E. Diller, "Resonance-based design of wireless magnetic capsule for effective sampling of microbiome in gastrointestinal tract," *Sensors and Actuators A: Physical*, vol. 342, p. 113654, 8 2022.

[9] B. J. Nelson, S. Gervasoni, P. W. Chiu, L. Zhang, and A. Zemmar, "Magnetically actuated medical robots: An in vivo perspective," *Proceedings of the IEEE*, vol. 110, pp. 1028–1037, July 2022.

[10] A. Hong, A. J. Petruska, A. Zemmar, and B. J. Nelson, "Magnetic control of a flexible needle in neurosurgery," *IEEE Transactions on Biomedical Engineering*, vol. 68, pp. 616–627, 2 2021.

[11] A. Lim, A. Schonewille, C. Forbrigger, T. Looi, J. M. Drake, and E. Diller, "Design and Comparison of Magnetically-Actuated Dexterous Forceps Instruments for Neuroendoscopy," *IEEE Transactions on Biomedical Engineering*, vol. 68, no. 3, pp. 846–856, Mar. 2021.

[12] H. M. Le, T. N. Do, and S. J. Phee, "A survey on actuators-driven surgical robots," *Sensors and Actuators, A: Physical*, vol. 247, pp. 323–354, 2016.

[13] C. Hong, Z. Ren, C. Wang, M. Li, Y. Wu, D. Tang, W. Hu, and M. Sitti, "Magnetically actuated gearbox for the wireless control of millimeter-scale robots," *Science Robotics*, vol. 7, p. eabo4401, 2022.

[14] M. Nica, C. Forbrigger, and E. Diller, "A novel magnetic transmission for powerful miniature surgical robots," *IEEE/ASME Transactions on Mechatronics*, pp. 1–10, 2022, DOI: 10.1109/TMECH.2022.3184599.

[15] H. J. Marcus, K. Zareinia, L. S. Gan, F. W. Yang, S. Lama, G.-Z. Yang, and G. R. Sutherland, "Forces exerted during microneurosurgery: a cadaver study," *International Journal of Medical Robotics and Computer Assisted Surgery*, vol. 10, no. 2, pp. 251–256, 2014.

[16] C. Forbrigger, A. Schonewille, and E. Diller, "Tailored Magnetic Torsion Springs for Miniature Magnetic Robots," in *IEEE International Conference on Robotics and Automation (ICRA)*. Xi'an, China: IEEE, June 2021, pp. 7182–7188.

[17] Y. Maddahi, A. Ghasemloonia, K. Zareinia, N. Sepehri, and G. R. Sutherland, "Quantifying force and positional frequency bands in neurosurgical tasks," *Journal of Robotic Surgery*, vol. 10, pp. 97–102, June 2016.

[18] R. Featherstone and D. E. Orin, "Dynamics," in *Springer Handbook of Robotics*, B. Siciliano and O. Khatib, Eds. Springer International Publishing, 2016, pp. 35–65.

[19] J. J. Abbott, E. Diller, and A. J. Petruska, "Magnetic Methods in Robotics," *Annual Review of Control, Robotics, and Autonomous Systems*, vol. 3, pp. 57–90, 2020.

[20] M. A. Woodward and M. Sitti, "Universal Custom Complex Magnetic Spring Design Methodology," *IEEE Transactions on Magnetics*, vol. 54, no. 1, p. 8200213, Jan. 2018.

[21] ——, "Tailored Magnetic Springs for Shape-Memory Alloy Actuated Mechanisms in Miniature Robots," *IEEE Transactions on Robotics*, vol. 35, no. 3, pp. 589–601, June 2019.

[22] S. Salmanipour, O. Youssefi, and E. Diller, "Design of Multi-Degree-of-Freedom Microrobots Driven by Homogeneous Quasi-Static Magnetic Fields," *IEEE Transactions on Robotics*, vol. 37, no. 1, pp. 246–256, Feb. 2020.

[23] J.-J. E. Slotine and W. Li, *Applied Nonlinear Control*. Prentice-Hall Inc., 1991.

[24] B. Jacob and G. Guennebaud. (2022, Apr.) Eigen 3.4. [Online]. Available: https://eigen.tuxfamily.org/dox/

[25] L. L. Howell, S. P. Magleby, and B. M. Olsen, *Handbook of Compliant Mechanisms*. John Wiley & Sons, Inc., 2013.

[26] A. Schonewille, "Maximizing Workspace Accessibility in Magnetic Actuation of Tethered Microsurgical Tools Using Non-Uniform Magnetic Fields," MASc Thesis, University of Toronto, 2022.

[27] T. Hägglund, *Reglerteknik AK, Föreläsningar*. KFS i Lund AB, 2015.

[28] N. Simaan, R. M. Yasin, and L. Wang, "Medical technologies and challenges of robot-assisted minimally invasive intervention and diagnostics," *Annual Review of Control, Robotics, and Autonomous Systems*, vol. 1, pp. 15.1–15.26, May 2018.

[29] Y. Wang, Q. Sun, Z. Liu, and L. Gu, "Visual detection and tracking algorithms for minimally invasive surgical instruments: A comprehensive review of the state-of-the-art," *Robotics and Autonomous Systems*, vol. 149, 2022.

[30] M. Allan, S. Ourselin, D. J. Hawkes, J. D. Kelly, and D. Stoyanov, "3-d pose estimation of articulated instruments in robotic minimally invasive surgery," *IEEE Transactions on Medical Imaging*, vol. 37, pp. 1204–1213, 5 2018.

[31] J. Hein, M. Seibold, F. Bogo, M. Farshad, M. Pollefeys, P. Fürnstahl, and N. Navab, "Towards markerless surgical tool and hand pose estimation," *International Journal of Computer Assisted Radiology and Surgery*, vol. 16, pp. 799–808, 5 2021.